Quantum Science and Technology

PAPER • **OPEN ACCESS**

Heat transport in the quantum Rabi model: universality and ultrastrong coupling effects

To cite this article: L Magazzù *et al* 2025 *Quantum Sci. Technol.* **10** 025013

IOP Publishing Quantum Sci. Technol. 10 (2025) 025013 https://doi.org/10.1088/2058-9565/adae2c

Quantum Science and Technology

OPEN ACCESS

RECEIVED
30 September 2024

REVISED
8 January 2025

ACCEPTED FOR PUBLICATION
24 January 2025

PUBLISHED
4 February 2025

PAPER

Heat transport in the quantum Rabi model: universality and ultrastrong coupling effects

L Magazzù[1,*], **E Paladino**[2,3,4] **and M Grifoni**[1]

[1] Institute for Theoretical Physics, University of Regensburg, 93040 Regensburg, Germany
[2] Dipartimento di Fisica e Astronomia Ettore Majorana, Università di Catania, Via S. Sofia 64, I-95123 Catania, Italy
[3] INFN, Sez. Catania, I-95123 Catania, Italy
[4] CNR-IMM, Via S. Sofia 64, I-95123 Catania, Italy
[*] Author to whom any correspondence should be addressed.

E-mail: luca.magazzu@physik.uni-regensburg.de

Keywords: quantum transport, ultrastrong coupling, open quantum systems

Abstract

Heat transport in a qubit–oscillator junction described by the quantum Rabi model is investigated. Upon variation of temperature, bias on the qubit and the qubit–oscillator coupling strength, a rich variety of effects is identified. For weak coupling to bosonic heat baths, transport is essentially controlled by the qubit–oscillator coupling g which defines a Kondo-like temperature $T_{\rm K}(g)$. At temperatures much lower than $T_{\rm K}$, coherent heat transfer via virtual processes yields a T^3 behavior in the linear conductance as a function of T, modulated by a prefactor determined by the junction parameters and unravelling its multilevel nature. In particular, a coherent suppression of the conductance arises in the presence of quasi-degeneracies in the spectrum. For $T \gtrsim T_{\rm K}$, sequential processes dominate heat transfer and a scaling regime is found when quantities are scaled with $T_{\rm K}$. The conductance as a function of the bias on the qubit undergoes a transition from a resonant behavior at weak qubit–resonator coupling to a broadened, zero-bias peak regime at ultrastrong coupling.

1. Introduction

Qubit–resonator systems constitute the building block of circuit-QED platforms [1]. They are modelled as two-level systems (TLSs) coupled to quantum harmonic oscillators according to the celebrated quantum Rabi model [2, 3] and its generalizations. Superconducting circuit realizations of the Rabi model allow for tunable light-matter coupling strengths reaching the ultrastrong coupling (USC) regime, where the frequency associated to the qubit–resonator coupling is of the same order of magnitude as the qubit/resonator frequencies [4–9].

Recent experiments have demonstrated the control of photonic heat current between heat baths contacted via composite superconducting qubit–resonator junctions [10–12]. The latter can display a heat valve behavior upon modulation of the parameters [13, 14]. Due to the intrinsic nonlinearity of the qubits, these junction can behave as heat rectifiers, provided that the coupling to the baths is asymmetric [15–20]. As such, these platforms appear to be ideal for demonstrating different heat transport regimes and effects with a single device.

A varied picture of heat transport effects and regimes is already found in the simpler setup of an individual TLS coupled directly with strength α to bosonic heat baths, collectively embodying the spin-boson model (SBM) [21, 22]. Heat transport in the SBM has been theoretically studied in the whole temperature range, using both weak-coupling analytical methods and nonperturbative analytical and numerical techniques [15, 23–31]. The thermal conductance κ exhibits, in the Ohmic SBM , a scaling behavior as a function of $T/T_{\rm K}$, with $T_{\rm K} = T_{\rm K}(\alpha) = \hbar\tilde{\Delta}(\alpha)/k_{\rm B}$ a characteristic Kondo temperature given by the bath-renormalized qubit frequency splitting $\tilde{\Delta}(\alpha) = [\Gamma(1-2\alpha)\cos(\pi\alpha)]^{[1/2(1-\alpha)]}\Delta(\Delta/\omega_{\rm c})^{\alpha/(1-\alpha)}$

($\alpha < 1$) [25]. Here Δ is the bare TLS frequency, $\Gamma(x)$ is the Gamma function, and ω_c is the frequency cutoff of the baths spectral density function [22].

At low temperatures, $T \ll T_K$, heat transport occurs via coherent processes yielding the universal power-law for the thermal conductance $\kappa(T) \sim T^3$. Note that, even at weak system-bath coupling, these processes can only be captured by beyond-leading order approaches [23, 31]. At intermediate-to-high temperatures, incoherent absorption/emission processes defining the so-called sequential regime are dominant, and yield the coupling-dependent, high-temperature power law $\kappa(T) \sim T^{2\alpha-1}$ [25, 31].

While heat transport is by now well understood for the SBM, fewer theory works have addressed the more involved problem of heat transport in nonlinear, multilevel junctions where the qubit is connected to one or both baths via resonators. A natural question is to which extent heat transport in generalized Rabi models is affected by the internal couplings among its constituents. This issue was recently addressed in [32] for a junction embodying the quantum Rabi model with longitudinal and transverse qubit–resonator coupling. An optimal mixing angle between longitudinal and transverse coupling is found which maximizes the heat current in the sequential regime. Inspired by the experimental results on the heat valve effect in [14], Xu *et al* investigated a setup where a qubit of tunable frequency is weakly connected to heat baths via identical resonators [33]. Using the numerical method of hierarchical equations of motion and perturbative weak-coupling schemes, they reproduced the occurrence of distinct resonant features, affected by the presence of a direct oscillator–oscillator coupling. A similar model was also investigated in [34], but with no direct coupling between the oscillators. This allows for a mapping to the SBM with so-called structured heat baths, which are peaked at the resonators' frequency [35, 36]. Interestingly, a low-temperature behavior $\kappa(T) \sim T^3$ was found, like in the Ohmic SBM [23, 31], followed by a double peak at higher temperatures and in the USC regime.

The above examples show that heat transport in generalized Rabi models is very rich, with effects which could depend on details of the internal structure of the junctions. At the same time though, results like in [31] hint at features which might be universal, and largely model-independent.

In this work we investigate heat transport in the quantum Rabi model and demonstrate the low-temperature T^3 law for generic qubit–resonator coupling. As the temperature is increased, the linear conductance even exhibits a scaling behavior, similar to the simpler Ohmic SBM. Multilevel features manifest themselves e.g. in interference effects at the lowest temperatures. Part of these results are also discussed in our recent methodological work [37], where the diagrammatic transport theory used here has been developed. The latter allows for the investigation of nonlinear heat transport in circuit-QED platforms beyond leading order in the system-bath coupling. Here, we focus on linear transport at weak coupling to the heat baths, addressing the different transport regimes emerging by varying temperature, the internal qubit–oscillator coupling, and a static bias applied to the qubit. We calculate the thermal conductance beyond leading order, i.e. up to fourth-order in the system-bath coupling, as required to capture the virtual processes enabling heat transport at low temperature.

The main findings of the present work are summarized as follows. Weak coupling α to the heat baths entails that the renormalization effects induced by the coupling to the latter are negligible and a prominent role in determining the characteristic frequencies of the junction is played by the coupling strength g. Accounting for the multilevel nature of the model and the large qubit–oscillator entanglement at USC, a characteristic Kondo-like temperature $T_K = T_K(g)$ is identified, in terms of which distinct transport regimes are recognized. At temperatures much below T_K coherent processes involving virtual photons dominate transport, and the power-law dependence $\kappa(T) \sim T^3$ of the conductance as a function of T is found, similarly to the case of the SBM. In contrast to the SMB however, the multilevel nature of the Rabi model manifests itself in destructive interference in the presence of quasi-degeneracies in the spectrum, resulting in a suppression of the conductance. This behavior can also be found in other multilevel systems, non necessarily nonlinear, e.g. coupled harmonic oscillators [37]. For temperatures around T_K, the conductance exhibits a scaling behavior as a function of T. Moreover, under suitable conditions, nonvanishing steady-state coherences induce a suppression of the conductance. This is another coherent multilevel effect, this time appearing in the sequential regime. A further multilevel effect, in this case incoherent, occurs at high temperature: the thermal conductance does not show a power-low behavior, but depends on the junction parameters, namely on the details of the spectrum of the Rabi model. This is due to excited levels higher than the first having nonnegligible steady-state populations. Finally, when plotted vs the qubit bias, the thermal conductance in the sequential tunneling regime exhibits a resonant behavior at small g, with the conductance peaking when the resonance condition between the qubit and the resonator is met, while displaying a zero-bias maximum in the USC regime. These findings show that the internal coupling g in the open quantum Rabi model at small α plays a similar role as the coupling strength α of the SBM in the appropriate temperature regime. In addition, they suggest a universal behavior of the low-temperature thermal conductance of generic multilevel quantum systems weakly coupled to bosonic Ohmic baths.

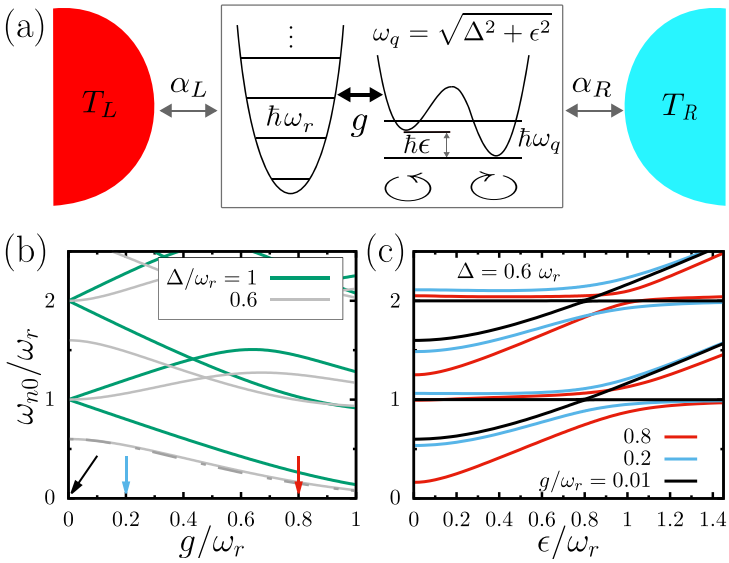

Figure 1. Heat transport setup and excitation spectrum of the Rabi model. (a) - A flux qubit–resonator system is weakly coupled to independent Ohmic baths. The circular arrows indicate left/right-circulating persistent current states. (b) and (c) — Excitation spectrum of the Rabi model vs qubit–resonator coupling g at zero bias and vs the qubit bias ϵ at $\Delta = 0.6\,\omega_{\rm r}$. The arrows in panel (b) highlight the values of g used in panel (c). Solid lines are numerical evaluations while the dashed–dotted line is given by the approximate expression (2).

2. Setup

A scheme of the heat transport setup considered in this work is provided in figure 1. The junction is formed of a superconducting qubit coupled to a resonator. Exemplarily, we consider a flux qubit, where the qubit frequency $\omega_{\rm q} = \sqrt{\Delta^2+\epsilon^2}$ can be modulated by an applied bias ϵ. The resonator is modeled as a quantum oscillator of frequency $\omega_{\rm r}$. A circuit schematic for this setup is provided in section 5 below. This system is described by the biased Rabi Hamiltonian which, in the basis of the qubit persistent current states $\{|\circlearrowright\rangle, |\circlearrowleft\rangle\}$, has the form [4, 5]

$$\hat{H}_{\rm Rabi} = -\frac{\hbar}{2}\left(\epsilon\hat{\sigma}_z + \Delta\hat{\sigma}_x\right) + \hbar\omega_{\rm r}\hat{a}^\dagger\hat{a} + \hbar g\hat{\sigma}_z\left(\hat{a}^\dagger + \hat{a}\right)\,. \tag{1}$$

Here, $\hat{a}^\dagger$ ($\hat{a}$) creates (annihilates) an excitation of the field mode in the resonator while $\hat{\sigma}_z = |\circlearrowright\rangle\langle\circlearrowright| - |\circlearrowleft\rangle\langle\circlearrowleft|$ and $\hat{\sigma}_x = |\circlearrowright\rangle\langle\circlearrowleft| + |\circlearrowleft\rangle\langle\circlearrowright|$ are the Pauli spin operators.

To understand the transport properties to be discussed later, it is important to discuss the excitation spectrum of the Rabi model shown in figures 1(b) and (c) as a function of the coupling g and bias ϵ, respectively. The nonperturbative USC regime is attained for $0.3 \lesssim g/\omega_{\rm r} \lesssim 1$[5], and is characterized by a large qubit–oscillator entanglement in the ground state at zero bias [38]. At weak-to-intermediate coupling, $g/\omega_{\rm r} \lesssim 0.3$, doublets can be recognized at resonance $\omega_{\rm q}/\omega_{\rm r} = 1$. In appendix A we review some analytical approximation schemes for the diagonalization the Rabi Hamiltonian in different parameter regimes. The second-order Van Vleck perturbation theory (VVPT) in g [39] correctly describes the Rabi model for arbitrary $\Delta/\omega_{\rm r}$. Its weak coupling limit reproduces the rotating wave approximation (RWA). On the other hand,the generalized RWA (GRWA) [40, 41] is valid for arbitrary g and $\Delta/\omega_{\rm r} \lesssim 1$. As we shall see, the frequency ω_{10}, where $\omega_{nm} = (E_n - E_m)/\hbar$, gives the Kondo-like temperature via $T_{\rm K} = \hbar\omega_{10}/k_{\rm B}$. Within the GRWA, the frequency gap ω_{10} at zero bias is approximated by

$$\omega_{10}(g) \simeq \Delta e^{-\tilde{\alpha}/2} - \frac{\delta}{2} - \frac{1}{2}\sqrt{\delta^2 + \tilde{\alpha}\left(\Delta e^{-\tilde{\alpha}/2}\right)^2}\,, \tag{2}$$

where $\delta := \Delta e^{-\tilde{\alpha}/2}(2-\tilde{\alpha})/2 - \omega_{\rm r}$ and where $\tilde{\alpha} := (2g/\omega_{\rm r})^2$ is the *internal* effective coupling. The dashed-dotted line in figure 1(b) reproduces $T_{\rm K}$, according to equation (2), for $\Delta = 0.6\,\omega_{\rm r}$. As can be seen

[5] In the USC literature, the coupling strength g is compared to the loss rates of the system and its characteristic frequencies [7]. To simplify the discussion, and in view of the very small coupling to the heat baths assumed here, we define the coupling regimes based solely on the ratio $g/\omega_{\rm r}$. In particular, while the USC already sets in for $g/\omega_{\rm r} \simeq 0.1$, throughout the text by USC we mean the nonperturbative USC regime $0.3 \lesssim g/\omega_{\rm r} \lesssim 1$ [6].

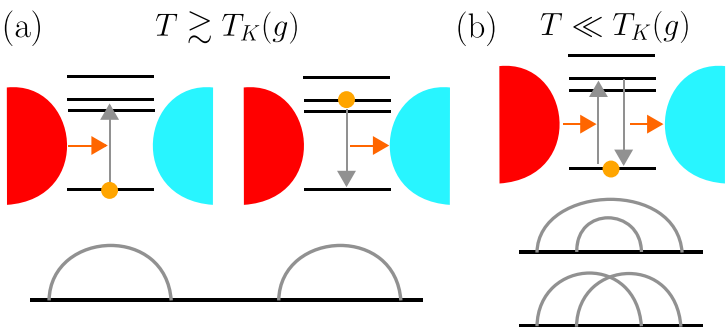

Figure 2. Relevant mechanisms for heat transfer, starting and ending in the ground state of the Rabi model. Sequential (a) and coherent (b) transport and the corresponding diagrammatic contributions to the current, which dominate above and below the Kondo temperature $T_K(g)$, respectively. The orange bullets indicate occupation of an energy level of the Rabi model.

from equation (A22), for vanishing g and $\Delta < \omega_r$ the Kondo-like temperature approaches the bare qubit splitting, $\omega_{10} = \Delta$, while in the opposite limit of large g/ω_r it is suppressed as $\omega_{10} \simeq \Delta e^{-\tilde{\alpha}/2}$.

In the minimal setup for heat transport, the junction, described in our case by the quantum Rabi model, is connected to two heat baths, possibly at different temperatures. The Hamiltonian of the two-bath setup reads [42, 43]

$$\hat{H} = \bar{H}_{\rm Rabi} + \sum_{l=R,L} \left(\hat{H}_l + \hat{Q}_l \hat{B}_l \right) . \tag{3}$$

The second and third terms collect the baths' Hamiltonians $\hat{H}_l = \sum_j \hbar\omega_{lj} \hat{b}_{lj}^\dagger \hat{b}_{lj}$ and the coupling of the system with the individual bath modes, respectively, via the bath displacement operators $\hat{B}_l \equiv \sum_j \hbar\lambda_{lj}(\hat{b}_{lj} + \hat{b}_{lj}^\dagger)$ according to the Caldeira–Leggett model [44, 45]. The coupling is mediated by the dimensionless system operators $\hat{Q}_L = \hat{a} + \hat{a}^\dagger$ and $\hat{Q}_R = \hat{\sigma}_z$. The baths and their interaction with the system are collectively described by the spectral density functions $J_l(\omega) = \sum_{j=1}^N \lambda_{lj}^2 \delta(\omega - \omega_j)$. In the continuum limit, the Ohmic case has the low-frequency behavior $J_l(\omega) \sim \alpha_l \omega$, where α_l measures the coupling to bath l. Finally, $\bar{H}_{\rm Rabi} = \hat{H}_{\rm Rabi} + \sum_l \hbar \int_0^\infty {\rm d}\omega [J_l(\omega)/\omega] \hat{Q}_l^2$ incorporates the bath-induced renormalization[6].

3. Quantum heat transport

The heat current $I_l(t)$ to bath l is defined as the expectation value of the current operator $\hat{I}_l = {\rm d}\hat{H}_l(t)/{\rm d}t = {\rm i}\hat{Q}_l \sum_j \lambda_{lj}\hbar\omega_{lj}[\hat{b}_{lj} - \hat{b}_{lj}^\dagger]$, namely $I_l(t) = \langle \hat{I}_l(t) \rangle$. For its evaluation, we use the diagrammatic approach in Liouville space described in [37]. It generalizes to bosonic reservoirs the Liouville formalism typically used for electronic transport in nanojunctions, see [46]. The steady-state reduced density matrix and heat current to bath l are the solutions of the exact equations

$$0 = \mathcal{L}_{\rm Rabi} \hat{\rho}^\infty + \tilde{\mathcal{K}}(0)\, \hat{\rho}^\infty \quad \text{and} \quad I_l = {\rm Tr} \left[\tilde{\mathcal{K}}_{Il}(0)\, \hat{\rho}^\infty \right] . \tag{4}$$

Here, $\mathcal{L}_{\rm Rabi}$ and ρ^∞ are the Liouvillian superoperator and the steady-state reduced density matrix associated to the Rabi model, while $\tilde{\mathcal{K}}(0)$ and $\tilde{\mathcal{K}}_{Il}(0)$ are the Laplace-transformed dynamical and current kernel superoperators, respectively [46]. The trace is with respect to the junction degrees of freedom. The current is calculated by solving for $\hat{\rho}^\infty$ using the first of equation (4) and plugging the solution in the second. The linear thermal conductance follows as

$$\kappa = \lim_{\Delta T \to 0} \frac{\partial}{\partial \Delta T} I_l \, . \tag{5}$$

where ΔT is the temperature difference between the baths such that the current to bath l is positive.

At weak Ohmic coupling α, heat transport is dominated by processes of second- and fourth-order in the system-bath coupling, depending on the temperature regime, see figure 2. The former describe sequential absorption and emission of bath excitations which dominate heat transport down to temperatures $T \lesssim T_{\rm K}$. For $T \ll T_{\rm K}$ though, due to the exponential suppression of excited-state populations, fourth-order processes constitute the main transport mechanism. In this case, heat transfer is mediated by *virtual* transitions to

[6] The renormalization term from the right bath coupled to the qubit ($\hat{Q}_R = \hat{\sigma}_z$) is a constant shift as $\hat{\sigma}_z^2 = \mathbb{I}$.

excited states dubbed 'cotunneling' processes in analogy with the electron transport counterpart [19, 23, 26, 31]. As we demonstrate below, the conductance of the Rabi system displays a universal power-law $\kappa \propto T^3$ at low temperature and a scaling behavior in the sequential regime.

The second-order conductance $\kappa^{(2)}$ is calculated using in equation (5) the current $I^{(2)}$ as given by equation (4) with the kernels up to second order in the coupling with the baths. An equivalent method was developed in [47] and applied to anharmonic molecular junctions. In the TLS truncation of the multilevel qubit–oscillator system formed by the ground and the first excited state of the Rabi Hamiltonian, and characterized by the frequency ω_{10}, the second-order conductance reads

$$\kappa^{(2)}_{\rm TLS} = \alpha\eta k_{\rm B}^2 T_{\rm K} \frac{(T_{\rm K}/T)^2}{2\hbar \sinh(T_{\rm K}/T)} , \tag{6}$$

where $\eta := 2\pi\, Q^2_{L,01} Q^2_{R,01}/(Q^2_{L,01} + Q^2_{R,01})$ is a dimensionless asymmetry factor. Notice that the couplings $Q_{l,01}$, and hence η, depend on g. At low temperatures, where essentially only the ground state of the Rabi system is populated, we find for the fourth-order contribution to the conductance of the full Rabi model the simple limiting expression [37]

$$\kappa^{(4)} \simeq \frac{32\alpha^2\pi^5 k_{\rm B}^4 T^3}{15\hbar^3} \sum_{k,m(\neq 0)} \frac{Q_{R,m0} Q_{L,0m} Q_{L,0k} Q_{R,k0}}{\omega_{m0}\omega_{k0}} . \tag{7}$$

The above formula predicts a $\sim T^3$ behavior for the multilevel system at hand, modulated by the sum over the system's states; the latter yields interference effects in the presence of quasi-degeneracies. In the TLS truncation, equation (7) simplifies to

$$\kappa^{(4)}_{\rm TLS} \simeq \frac{32\alpha^2\pi^5 k_{\rm B}^2 (T/T_{\rm K})^3}{15\hbar^3} Q^2_{L,10} Q^2_{R,10} T_{\rm K} . \tag{8}$$

Formally, this expression coincides with the known form of the low-temperature, weak-coupling conductance of the SBM. However, besides the coupling operators $\hat{Q}_l$ being different, in the present case $T_{\rm K} = T_{\rm K}(g)$, namely the Kondo-like temperature depends on the qubit–resonator coupling, while in the SBM it depends on the strength α of the coupling with the baths, i.e. $T_{\rm K} = T_{\rm K}(\alpha)$ [25, 31].

4. Universality, scaling, and interference

Numerical and analytical results for the linear conductance κ are shown in figures 3 and 4. They display the power-law behavior of equation (7), together with scaling properties of the conductance at moderate temperatures around $T_{\rm K}$. Furthermore, the emergence of a zero-bias maximum, signaling the transition to the USC regime, is observed in figure 4. We consider identical baths with Ohmic–Drude spectral density $J_l(\omega) = \alpha\omega/(1+\omega^2/\omega_{\rm c}^2)$, with $\alpha = 10^{-3}$, sufficiently small for a perturbative approach to be appropriate, and cutoff frequency $\omega_{\rm c} = 5\,\omega_{\rm r}$. Numerical results are obtained with truncation of the oscillator's Hilbert space to the first 10 levels.

We start from figure 3(a). It shows the conductance scaled with $T_{\rm K}(g)$ as a function of $T/T_{\rm K}$, for the three values of the qubit–resonator coupling highlighted in figure 1. Solid lines are the results for the full Rabi model while dashed lines refer to its TLS truncation. The curves in the center and right part of the panel (second order), showing exponential suppression at low T, are given by equations (5), with $I_l \simeq I_l^{(2)}$, and (6), while the ones with T^3 behavior (fourth order) in the left part of the panel and in the inset are obtained using the analytical limiting expressions (7) and (8) [7]. At small g, the excited spectrum of the Rabi model has the doublet structure shown in figure 1(b). This quasi-degeneracy results in *destructive interference* and in turn in the suppression of the low-temperature conductance by several orders of magnitude, as also seen in the inset of figure 3(a). Indeed, in equation (7), at resonance and weak coupling, $\omega_{10} \simeq \omega_{20}$ and $Q_{L,01} = Q_{L,02}$ while $Q_{R,01} = -Q_{R,02}$, see appendix A, leading to a suppression of $\kappa^{(4)}$. Analogously, the second-order conductance $\kappa^{(2)}$ in figure 3(a) is impacted by the presence, at small g, of the nonvanishing steady-state coherence ρ_{12} [37, 48] associated to the quasi-degenerate first- and second-excited levels. As a consequence, the black-solid curve is calculated using the partial secular master equation [37]. This can be considered as a finite system-bath coupling effect. Indeed, for vanishing α, second-order coherent effects vanish, as the elements of the kernels in equation (4) become small, even with respect to the quasi-degenerate Bohr

[7] In the region of overlap between the two curves the conductance is expected to be given by $\kappa = \kappa^{(2)} + \kappa^{(4)}$, with $\kappa^{(4)}$ calculated as a double frequency integral without the simplifying assumption of very low temperature. See [37] for more details.

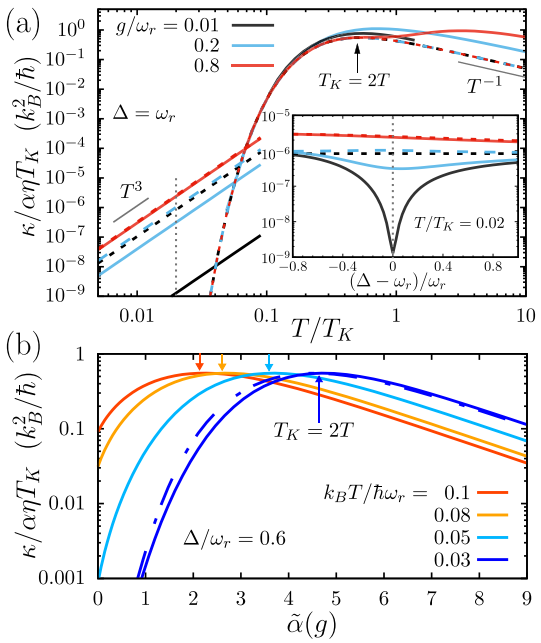

Figure 3. Universality and interference effects at zero qubit bias. (a) — Linear conductance *vs.* temperature for three values of the coupling g in the Rabi model (solid lines) and its TLS truncation (dashed lines). A universal power-law behavior is found for $T \ll T_K(g)$ when transport is governed by virtual processes. At moderate temperature, heat transport is incoherent and κ reaches a maximum for $T = T_K/2$. Inset—conductance *vs.* detuning at the low temperature indicated by the dotted vertical line in the main panel, where the detuning is zero. At resonance, for weak coupling, the first and second excited states are quasi-degenerate, see figure 1(b), yielding multilevel interference effects. (b) - Linear conductance *vs.* the effective coupling $\tilde{\alpha}(g) = (2g/\omega_r)^2$, see equation (2), for different temperatures (solid lines). The exponential decay of the conductance at large coupling reflects a corresponding suppression in T_K. Dashed–dotted line: Analytical result for $\kappa^{(2)}_{\rm TLS}$ within the GRWA.

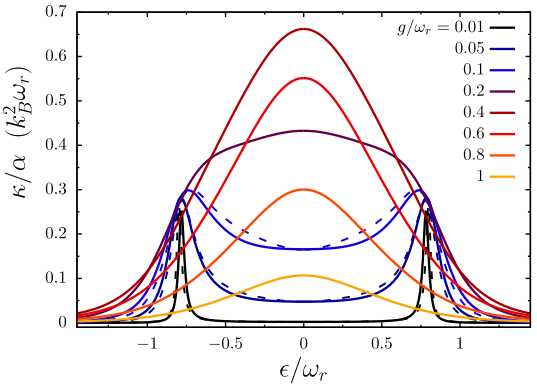

Figure 4. Transition from resonant to USC regime. Conductance vs the qubit bias for different values of the coupling g. At weak coupling, the conductance exhibits two sharp peaks at resonance, $\omega_{\rm q} = \omega_{\rm r}$. As the coupling is increased, a broadened, zero-bias peak emerges. It reflects that, at USC, the coupling between the qubit and the (right) heat bath is strongly suppressed at finite bias. Dashed lines: $\kappa^{(2)}$ in the full secular approximation within VVPT in g and truncation to the first four levels. The temperature is $k_{\rm B}T = 0.2\ \hbar\omega_{\rm r}$ and $\Delta/\omega_{\rm r} = 0.6$.

frequencies of the junction. Due to a truncation to 5 levels performed here, the partial secular master equation is not accurate at high temperature and therefore not shown in this regime. Obviously, these features are not observed in the SBM. In the opposite regime of USC, transport for $T \lesssim T_{\rm K}$ is rendered by the TLS truncation of the full Rabi model. This can be understood in terms of the clear separation in the excitation spectrum at intermediate-to-large values of g.

For temperatures $T < T_{\rm K}$, equation (6) gives $\kappa^{(2)}_{\rm TLS}/T_{\rm K} \propto \alpha\eta(T_{\rm K}^2/T^2)e^{-T_{\rm K}/T}$, yielding for the position of the maxima the condition $T = T_{\rm K}/2$. This also reproduces the position of the maxima in the full Rabi model, as shown in both panels of figure 3. At high temperatures, the TLS approximation breaks down at any g, since more levels of the Rabi model can contribute to transport.

In figure 3(b) the conductance is plotted against the effective coupling strength $\tilde{\alpha} = (2g/\omega_{\rm r})^2$ for different temperatures (in a range where the conductance is dominated by $\kappa^{(2)}$). Numerical evaluations in

the full Rabi model are compared to $\kappa^{(2)}_{\rm TLS}$ obtained within the GRWA. Remarkably, the results are qualitatively similar to those obtained in [25] for the conductance of a qubit *vs.* the qubit-bath coupling strength α. For large $\tilde{\alpha}$, the effective frequency ω_{10} is suppressed, so that the high-temperature expansion $\kappa^{(2)}_{\rm TLS} \propto \alpha\eta T_{\rm K}^2/T$ is appropriate. The GRWA expression for ω_{10} at zero bias gives $\omega_{10} \simeq \Delta\exp(-\tilde{\alpha}/2)$, and we obtain $\kappa^{(2)}_{\rm TLS} \propto \alpha\eta\Delta^2 {\rm e}^{-\tilde{\alpha}}/T$, which accounts for the exponential decay at large $\tilde{\alpha}$.

In figure 4, we provide numerical and semi-analytical (VVPT in g) results for the thermal conductance vs the detuning between qubit and resonator. Specifically, the effect of a flux bias ϵ applied to the qubit is considered for $\Delta = 0.6\,\omega_{\rm r}$. A transition from a resonant behavior at weak coupling to broadened zero-bias peaks in the USC regime is found. The curves show suppressed conductance at weak coupling, except for the peaks at resonance, $\omega_{\rm q} = \omega_{\rm r}$. In this regime, coherent effects impact the conductance, also at the level of second order, see appendix B. Upon increasing g, the conductance peaks broaden and move towards lower frequencies, $\omega_{\rm q} < \omega_{\rm r}$. Entering the nonperturbative USC regime of qubit–resonator coupling, a single, zero-bias peak emerges.

The features of the conductance in figure 4 can be accounted for by considering the spectrum and the matrix elements $Q_{l,01}$ of the coupling operators evaluated with the perturbative methods summarized in appendix A. In the weak coupling regime, the RWA predicts for the effective frequency $\omega_{10} = \omega_{\rm q} - \delta + \Omega/2$, with $\Omega := \delta - \sqrt{\delta^2 + 4g_x^2}$, detuning $\delta := \omega_{\rm q} - \omega_{\rm r}$, and $g_x := g\Delta/\omega_{\rm q}$. The relevant matrix elements are approximated by $Q_{L,01} = {\rm v}$ and $Q_{R,01} = {\rm u}\Delta/\omega_{\rm q}$, where ${\rm u} := \Omega/\sqrt{\Omega^2 + 4g_x^2}$, and ${\rm v} := -2g_x/\sqrt{\Omega^2 + 4g_x^2}$. Off-resonance, $\delta \gg g$, the conductance is suppressed as ${\rm v} \sim 0$, whereas at resonance ${\rm v} = {\rm u} = -1\sqrt{2}$, giving a peak in the conductance. This result is independent of g, which accounts for the pinning of the conductance at the resonance condition for different (small) values of $\tilde{\alpha}(g)$. Increasing the coupling, the peaks broaden and shift towards lower frequencies. This behavior is captured by VVPT in g, where the resonance condition is modified as $\omega_{\rm q} = \omega_{\rm r} - 2g_x^2/(\omega_{\rm q} + \omega_{\rm r})$, and is therefore attained at smaller $\omega_{\rm q}$, the larger the coupling g. The GRWA is well-suited for the USC regime and accounts for the zero-bias peak. Indeed, it gives for the matrix element of the qubit coupling operator $Q_{R,01} \simeq \Delta{\rm e}^{-\tilde{\alpha}/2}/\sqrt{\Delta^2{\rm e}^{-\tilde{\alpha}} + \epsilon^2}$, which is suppressed at finite bias. This behavior parallels the one found in the spectral function of the SBM [25], as a function of the frequency, upon increasing the qubit-bath coupling α.

An intuitive picture of the transition from the resonant to the USC regime depicted in figure 4 can be given by considering how the two components of the junction interact with each other and with the heat baths. At weak qubit–resonator coupling, an appropriate picture for the heat current is that of a sequence of processes where, for example, the hot bath excites the resonator and the latter transfers this excitation to the qubit which, in turn, is de-excited by transferring the excitation to the cold bath. This mechanism is effective at resonance, which accounts for the peaks. In the USC regime on the other hand, the resonator and the qubit form a highly-hybridized system and can no longer be considered as individual subsystems. The eigenstates can be indeed be expressed in terms of displaced resonator states with the displacement depending on the qubit state, equation (A17). When the bias is much larger than the renormalized qubit splitting, the qubit localized basis and the energy basis coincide, cf equations (1) and (A8). This is the case in the USC regime, where the renormalization of the qubit splitting is large: At large bias, the coupling operator to the baths (and to the resonator) is $\hat{\sigma}_z$ in both basis, which means that the interaction with the qubit does not induce transitions and transport is therefore hindered.

5. Superconducting circuit implementation

The the heat transport setup shown in figure 1 is based on the quantum Rabi model, with a static bias on the TLS, weakly coupled to bosonic heat baths. Here we provide the scheme of a possible implementation in a superconducting quantum circuit platform[8]. A simplified circuit scheme is given in figure 5. There, a flux qubit, biased by an applied magnetic flux $\phi_{\rm ext}$, is coupled to a superconducting LC oscillator via a shared, tunable inductance $L_{\rm c}$ [4, 5, 43]. The resulting circuit is inductively coupled to the heat reservoir l (with $l = L, R$) via the mutual inductance M_l [49–52]. The inductive coupling between the resonator and the left bath realizes a coupling with the individual jth mode of the bath of the type $(\hat{a}^\dagger + \hat{a})(\hat{b}_j^\dagger + \hat{b}_j)$, while the qubit-right bath inductive coupling yields a coupling of the type $\hat{\sigma}_z(\hat{b}_j^\dagger + \hat{b}_j)$ in the persistent current basis of equation (1) [51]. The qubit–resonator coupling strength is estimated via $g/\omega_{\rm r} = L_{\rm c}I_{\rm p}[2\hbar\omega_{\rm r}(L_{\rm c} + L_{\rm r})]^{-1/2}$ [5]. A coupling $g/\omega_{\rm r} \simeq 0.4$ can be attained with qubit persistent current $I_{\rm p} = 100$ nA, shared coupling inductance $L_{\rm c} = 1$ nH, resonator inductance $L_{\rm r} = 3.5$ nH, and resonator frequency $\omega_{\rm r}/2\pi = 10$ GHz. Following [52], an estimate for the strength of the coupling α_l between the system and the bath l is given by $\alpha_l = M_l I_{\rm p}/\sqrt{\hbar R_l}$, where R_l is the value of resistance of the resistive element of the circuit which forms the l

[8] See also [37] [cf figure 5(b) therein].

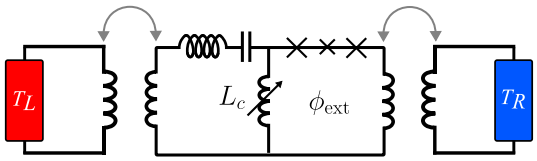

Figure 5. Superconducting circuit implementation of the heat transport setup in figure 1(a). The junction in the center is formed of a superconducting flux-type qubit (right part of the circuit, the symbol × denotes the Josephson junction) and a superconducting LC oscillator (left part). They are coupled via a tunable common inductance L_c. An applied flux $\phi_{\rm ext}$ induces a bias on the qubit. Each component of the junction is inductively coupled to a heat bath via mutual inductance M_l (gray arrows). The baths are implemented as dissipative circuits with resistive elements held at given temperatures T_l. Reprinted (figure) with permission from [37], Copyright (2024) by the American Physical Society.

heat bath. Setting $M_l = 10$ pH and $R_l = 1\ \Omega$ yields $\alpha_l \simeq 0.1$. Let us assume $\alpha_L = \alpha_R = 0.1$ and the junction parameters $\Delta/2\pi = \omega_{\rm r}/2\pi = 10$ GHz, $g/\omega_{\rm r} = 0.4$, and $\epsilon = 0$. Imposing a temperature bias $\Delta T = 0.2\ \hbar\omega_{\rm r}/k_{\rm B} \simeq 96$ mK, the current for $T = T_{\rm K} \simeq 290$ mK can be estimated via $I \simeq \kappa\Delta T$ (linear response) to be $I \simeq 27$ fW, which is within experimental reach [14]. For $T = 0.1\ T_{\rm K} \simeq 29$ mK and $\Delta T = 0.02\ \hbar\omega_{\rm r}/k_{\rm B} \simeq 9.5$ mK we have $I \simeq 17$ aW. Accessing the cotunneling regime occurring at even lower temperatures, see figure 3(a), can be expected to meet challenges in the design of the experiments.

6. Conclusions

We have shown how heat transport in a junction described by the quantum Rabi model and weakly coupled to the heat baths displays remarkable heat transport features. The rich picture emerging from the conductance encompasses a universal power-law behavior, multilevel interference effects, and scaling, together with a transition from a resonant, weak coupling regime to the USC regime characterized by a zero-bias maximum. The scaling behavior emerges when quantities are scaled with a Kondo-like temperature, which depends on the qubit–resonator coupling.

The quantum Rabi model, used as a junction in a heat transport setup, displays effects that are predicted in the SBM at strong coupling with the heat baths. This is attained while having the junction in a experimentally convenient weak coupling regime with the baths and tuning the internal qubit–resonator coupling in a range that is within reach of present experiments. In addition to this, the composite junction considered here can be easily brought in/out of resonance by applying an external bias: the heat valve effect results, at weak internal coupling, from the resonance peaks in the conductance, namely the conductance is almost completely suppressed out of resonance. At strong coupling, the conductance is significantly enhanced, beyond the peak values in the resonant regime, at intermediate coupling and at the qubit symmetry point. Finally, being an inherently multilevel junction, the qubit–oscillator system displays coherent effects at the steady state which arise in the presence of quasi-degenerate excited energy doublets. These effects result in a reduction of the conductance peaks in the sequential regime and large suppression of the cotunneling current by destructive interference. These effects are not present in a two-level-system junction.

Noticeably, our analysis even suggests that the power-law and scaling behavior of the heat conductance are a generic feature; it should be observable in other multilevel quantum systems coupled to bosonic baths, once the proper Kondo temperature is identified.

Data availability statement

The data that support the findings of this study are available upon reasonable request from the authors.

Acknowledgments

The authors thank A Donarini, G Falci, and J Pekola for fruitful discussions. LM and MG acknowledge financial support from BMBF (German Ministry for Education and Research), Project No. 13N15208, QuantERA SiUCs. The research is part of the Munich Quantum Valley, which is supported by the Bavarian state government with funds from the Hightech Agenda Bavaria. EP acknoweldges financial support from PNRR MUR Project PE0000023-NQSTI and from COST ACTION SUPQERQUMAP, CA21144.

Appendix A. Approximate diagonalization of the Rabi model

In this section, we provide the analytical approximate solutions of the quantum Rabi model used in the main text. First, we detail the second-order VVPT. Its first-order truncation gives the RWA. Secondly, the generalized RWA is described, where the perturbation parameter is the qubit splitting Δ dressed by the resonator.

A.1. Second-order VVPT in g

Let us define the frequency $\bar{\omega} = \omega_{\rm q} + \omega_{\rm r}$ and the couplings $g_z = g\epsilon/\omega_{\rm q}$ and $g_x = g\Delta/\omega_{\rm q}$. The latter are the longitudinal and transverse coupling, respectively, of the Rabi Hamiltonian expressed in the qubit energy basis. Within second-order VVPT in the qubit–resonator coupling g [39] the eigenenergies $E_n = \hbar\omega_n$ of the Rabi model read ($n \geqslant 1$)

$$\begin{aligned}
\omega_0 &= -\omega_{\rm q}^{(1)}/2 - g_z^2/\omega_{\rm r}\,, \\
\omega_{2n-1} &= -\frac{\omega_{\rm q}^{(n)}}{2} + \frac{\delta_n}{2} + n\omega_{\rm r} - \frac{g_z^2}{\omega_{\rm r}} - \frac{g_x^2}{\bar{\omega}} - \frac{1}{2}\sqrt{\delta_n^2 + 4ng_x^2}\,, \\
\omega_{2n} &= -\frac{\omega_{\rm q}^{(n)}}{2} + \frac{\delta_n}{2} + n\omega_{\rm r} - \frac{g_z^2}{\omega_{\rm r}} - \frac{g_x^2}{\bar{\omega}} + \frac{1}{2}\sqrt{\delta_n^2 + 4ng_x^2}\,,
\end{aligned} \tag{A1}$$

where $\omega_{\rm q}^{(n)} = \omega_{\rm q} + 2ng_x^2/\bar{\omega}$ and $\delta_n = \omega_{\rm q}^{(n)} - \omega_{\rm r}$. Note that this indexing provides the correct ordering of the eigenfrequencies only for small enough g, ϵ. The corresponding eigenvectors are

$$\begin{aligned}
|0\rangle &= |\widetilde{g,0}\rangle^{(2)}\,, \\
|2n-1\rangle &= {\rm u}_n^- |\widetilde{e,n-1}\rangle^{(2)} + {\rm v}_n^- |\widetilde{g,n}\rangle^{(2)}\,, \\
|2n\rangle &= {\rm u}_n^+ |\widetilde{e,n-1}\rangle^{(2)} + {\rm v}_n^+ |\widetilde{g,n}\rangle^{(2)}\,,
\end{aligned} \tag{A2}$$

where the coefficients are given by

$${\rm u}_n^\pm := \frac{\delta_n \pm \sqrt{\delta_n^2 + 4ng_x^2}}{\sqrt{\left(\delta_n \pm \sqrt{\delta_n^2 + 4ng_x^2}\right)^2 + 4ng_x^2}}\,, \qquad \text{and} \qquad {\rm v}_n^\pm := \frac{-2\sqrt{n}g_x}{\sqrt{\left(\delta_n \pm \sqrt{\delta_n^2 + 4ng_x^2}\right)^2 + 4ng_x^2}}\,. \tag{A3}$$

Note that in the main text we use the simplified notation ${\rm u}_1^- \equiv {\rm u}$ and ${\rm v}_1^- \equiv {\rm v}$.

The explicit form of the transformed states $|\widetilde{e/g,n}\rangle^{(2)}$ in terms of the uncoupled energy eigenbasis $\{|g,n\rangle, |e,n\rangle\}$ is

$$\begin{aligned}
\frac{|\widetilde{g,0}\rangle^{(2)}}{\mathcal{N}_{g,0}} &= |g,0\rangle + f(1)\,|e,0\rangle + \frac{g_z}{\omega_{\rm r}}|g,1\rangle + \frac{g_x}{\bar{\omega}}|e,1\rangle\,, \\
\frac{|\widetilde{g,n}\rangle^{(2)}}{\mathcal{N}_{g,n}} &= -\sqrt{n}\frac{g_z}{\omega_{\rm r}}|g,n-1\rangle + |g,n\rangle + f(n+1)\,|e,n\rangle + \sqrt{n+1}\frac{g_z}{\omega_{\rm r}}|g,n+1\rangle + \sqrt{n+1}\frac{g_x}{\bar{\omega}}|e,n+1\rangle \quad (n \geqslant 1)\,, \\
\frac{|\widetilde{e,0}\rangle^{(2)}}{\mathcal{N}_{e,0}} &= -f(1)\,|g,0\rangle + |e,0\rangle - \frac{g_z}{\omega_{\rm r}}|e,1\rangle, \\
\frac{|\widetilde{e,n}\rangle^{(2)}}{\mathcal{N}_{e,n}} &= -\sqrt{n}\frac{g_x}{\bar{\omega}}|g,n-1\rangle + \sqrt{n}\frac{g_z}{\omega_{\rm r}}|e,n-1\rangle - f(n+1)\,|g,n\rangle + |e,n\rangle - \sqrt{n+1}\frac{g_z}{\omega_{\rm r}}|e,n+1\rangle \quad (n \geqslant 1)\,,
\end{aligned} \tag{A4}$$

where $\mathcal{N}_i$ are the normalization factors and where $f(n) := (g_z g_x/\omega_{\rm r})[n/\omega_{\rm r} - (n-1)/\bar{\omega}]$.

A.1.1. Zero bias, $\epsilon = 0$

At zero bias, the ground and first excited state read

$$\begin{aligned}
|0\rangle &\propto |g,0\rangle + \frac{g}{\Delta + \omega_{\rm r}}|e,1\rangle\,, \\
|1\rangle &\propto {\rm u}_1^-|e,0\rangle + {\rm v}_1^-\left(|g,1\rangle + \frac{\sqrt{2}g}{\Delta + \omega_{\rm r}}|e,2\rangle\right)\,.
\end{aligned} \tag{A5}$$

The matrix elements of the system's coupling operators ($\hat{Q}_L = \hat{a} + \hat{a}^\dagger$ and $\hat{Q}_R = \sigma_z\epsilon/\omega_{\rm q} - \sigma_x\Delta/\omega_{\rm q}$, in the qubit energy basis) between the ground and first excited state read

$$Q_{L,01} \propto {\rm v}_1^-\left(1 + \frac{\sqrt{2}g}{\Delta + \omega_{\rm r}}\right) + {\rm u}_1^-\frac{g}{\Delta + \omega_{\rm r}}\,, \qquad Q_{R,01} \propto {\rm u}_1^- + {\rm v}_1^-\frac{g}{\Delta + \omega_{\rm r}}\,. \tag{A6}$$

The explicit expression for the coefficients is

$$\mathrm{u}_1^- := \frac{\delta_1 - \sqrt{\delta_1^2+4g^2}}{\sqrt{\left(\delta_1 - \sqrt{\delta_1^2+4g^2}\right)^2 + 4g^2}}\,, \qquad \text{and} \qquad \mathrm{v}_1^- := \frac{-2g}{\sqrt{\left(\delta_1 - \sqrt{\delta_1^2+4g^2}\right)^2 + 4g^2}}\,, \tag{A7}$$

where $\delta_1 = \Delta + 2g^2/(\Delta+\omega_\mathrm{r}) - \omega_\mathrm{r}$. Note that, at zero bias, these coefficients peak at the value of $\Delta < \omega_\mathrm{r}$ for which the condition $\delta_1 = 0$ is satisfied.

A.2. RWA

To first order in the coupling g, the VVPT expressions for the eigensystem of the quantum Rabi model, equations (A1)–(A5), reproduce the RWA results. The eigenstates of the system are, in this approximation, best given in terms of the qubit energy basis $\{|g\rangle, |e\rangle\}$. In this basis the Hamiltonian of the quantum Rabi model reads

$$H_\mathrm{Rabi} = -\frac{\hbar}{2}\omega_\mathrm{q}\hat{\sigma}_z + \hbar\omega_\mathrm{r}\hat{a}^\dagger\hat{a} + \hbar\left(g_z\hat{\sigma}_z - g_x\hat{\sigma}_x\right)\left(\hat{a}^\dagger + \hat{a}\right)\,, \tag{A8}$$

with $\omega_\mathrm{q} := \sqrt{\Delta^2+\epsilon^2}$ and the interaction terms with longitudinal and transverse couplings $g_z = g\epsilon/\omega_\mathrm{q}$ and $g_x = g\Delta/\omega_\mathrm{q}$. The Pauli matrices read $\hat{\sigma}_z = |g\rangle\langle g| - |e\rangle\langle e|$ and $\hat{\sigma}_x = \hat{\sigma}_+ + \hat{\sigma}_- = |g\rangle\langle e| + |e\rangle\langle g|$. Neglecting in equation (A8) the so-called counter-rotating terms $\hat{\sigma}_-\hat{a}$ and $\sigma_+ a^\dagger$ yields a 2×2 block-diagonal form, where the blocks have fixed excitation number. The resulting spectrum is

$$\begin{aligned}
\omega_0 &= -\omega_\mathrm{q}/2\,,\\
\omega_{2n-1} &= \left(n-\frac{1}{2}\right)\omega_\mathrm{r} - \frac{1}{2}\sqrt{\delta^2+n4g_x^2}\,,\\
\omega_{2n} &= \left(n-\frac{1}{2}\right)\omega_\mathrm{r} + \frac{1}{2}\sqrt{\delta^2+n4g_x^2}\,,
\end{aligned} \tag{A9}$$

($n \geqslant 1$), with the detuning δ defined as $\delta := \omega_\mathrm{q} - \omega_\mathrm{r}$. The corresponding eigenstates, in the energy basis of the uncoupled system, are

$$\begin{aligned}
|0\rangle &= |g,0\rangle\,,\\
|2n-1\rangle &= \mathrm{u}_n^-|e,n-1\rangle + \mathrm{v}_n^-|g,n\rangle\,,\\
|2n\rangle &= \mathrm{u}_n^+|e,n-1\rangle + \mathrm{v}_n^+|g,n\rangle\,,
\end{aligned} \tag{A10}$$

with coefficients

$$\mathrm{u}_n^\pm := \frac{\delta \pm \sqrt{\delta^2+n4g_x^2}}{\sqrt{\left(\delta \pm \sqrt{\delta^2+n4g_x^2}\right)^2 + n4g_x^2}}\,, \qquad \text{and} \qquad \mathrm{v}_n^\pm := \frac{-\sqrt{n}2g_x}{\sqrt{\left(\delta \pm \sqrt{\delta^2+n4g_x^2}\right)^2 + n4g_x^2}}\,. \tag{A11}$$

Within the RWA, the relevant matrix elements of the system's coupling operators ($\hat{Q}_L = \hat{a}+\hat{a}^\dagger$ and $\hat{Q}_R = \sigma_z\epsilon/\omega_\mathrm{q} - \sigma_x\Delta/\omega_\mathrm{q}$, in the qubit energy basis) read

$$\begin{aligned}
Q_{L,01} &= \mathrm{v}_1^-\,, \qquad & Q_{R,01} &= \mathrm{u}_1^-\frac{\Delta}{\omega_\mathrm{q}}\\
Q_{L,02} &= \mathrm{v}_1^+\,, \qquad & Q_{R,02} &= \mathrm{u}_1^+\frac{\Delta}{\omega_\mathrm{q}}.
\end{aligned} \tag{A12}$$

At resonance and for zero bias, $Q_{L,01} = Q_{L,02} = -1/\sqrt{2}$ while $Q_{R,01} = -Q_{R,02} = -1/\sqrt{2}$. If $\omega_{10} \simeq \omega_{02}$, the change of sign of the qubit matrix element yields the suppressed fourth-order conductance at weak coupling, see equation (7) and figure 3. Note that the RWA is the exact solution of the Jaynes–Cummings model [53].

A.2.1. GRWA

Within the GRWA [40, 41], the spectrum $E_n = \hbar\omega_n$ of the biased Rabi model is approximated by

$$\begin{aligned}
\omega_0 &= -\omega_{q,0}/2 - g^2/\omega_\mathrm{r}\,,\\
\omega_{2n-1} &= -\frac{\omega_{q,n}}{2} + \frac{\delta_n}{2} + n\omega_\mathrm{r} - \frac{g^2}{\omega_\mathrm{r}} - \frac{1}{2}\sqrt{\delta_n^2+\Omega_n^2}\,,\\
\omega_{2n} &= -\frac{\omega_{q,n}}{2} + \frac{\delta_n}{2} + n\omega_\mathrm{r} - \frac{g^2}{\omega_\mathrm{r}} + \frac{1}{2}\sqrt{\delta_n^2+\Omega_n^2}\,.
\end{aligned} \tag{A13}$$

Here, $\delta_n := (\omega_{q,n}+\omega_{q,n-1})/2-\omega_{\rm r}$, $\omega_{q,n} := \sqrt{\tilde{\Delta}_{nn}^2+\epsilon^2}$, and $\Omega_n := \tilde{\Delta}_{nn-1}(c_n^+c_{n-1}^+ + c_n^-c_{n-1}^-)$, where $c_n^\pm := \sqrt{(\omega_{q,n}\pm\epsilon)/2\omega_{q,n}}$. Here, we have introduced the dressed qubit gap $\tilde{\Delta}_{ij} = \Delta e^{-\tilde{\alpha}/2}\tilde{\alpha}^{(i-j)/2}\sqrt{j!/i!}\,\mathsf{L}_j^{i-j}(\tilde{\alpha})$ $(i\geqslant j)$, where $\tilde{\alpha} := (2g/\omega_{\rm r})^2$ and where L_n^k are the generalized Laguerre polynomials defined by the recurrence relation

$$\mathsf{L}_{j+1}^k(\tilde{\alpha}) = \frac{(2j+1+k-\tilde{\alpha})\mathsf{L}_j^k(\tilde{\alpha}) - (j+k)\mathsf{L}_{j-1}^k(\tilde{\alpha})}{j+1}\,, \tag{A14}$$

with $\mathsf{L}_0^k(\tilde{\alpha})=1$ and $\mathsf{L}_1^k(\tilde{\alpha}) = 1+k-\tilde{\alpha}$. The corresponding energy eigenstates are

$$\begin{aligned} |0\rangle &= |\Psi_{+,0}\rangle\,,\\ |2n-1\rangle &= \mathrm{u}_n^-|\Psi_{-,n-1}\rangle + \mathrm{v}_n^-|\Psi_{+,n}\rangle\,,\\ |2n\rangle &= \mathrm{u}_n^+|\Psi_{-,n-1}\rangle + \mathrm{v}_n^+|\Psi_{+,n}\rangle\,, \end{aligned} \tag{A15}$$

with the weights given by

$$\mathrm{u}_n^\pm := \frac{\delta_n \pm \sqrt{\delta_n^2+\Omega_n^2}}{\sqrt{\left(\delta_n\pm\sqrt{\delta_n^2+\Omega_n^2}\right)^2+\Omega_n^2}}\,, \qquad \text{and} \qquad \mathrm{v}_n^\pm := \frac{-\Omega_n}{\sqrt{\left(\delta_n\pm\sqrt{\delta_n^2+\Omega_n^2}\right)^2+\Omega_n^2}}\,. \tag{A16}$$

The states

$$|\Psi_{\pm,j}\rangle = c_j^\mp|-_z j_-\rangle \pm c_j^\pm|+_z j_+\rangle \tag{A17}$$

are superpositions of the displaced states $|\pm_z j_\pm\rangle = \exp[g\sigma_z(a-a^\dagger)/\omega_{\rm r}]|\pm_z\rangle|j\rangle \equiv |\pm_z\rangle D(\pm g/\omega_{\rm r})|j\rangle$, where $\{|\pm_z\rangle\}$ is the qubit localized basis, i.e. $\{|+_z\rangle,|-_z\rangle\}\equiv\{|\circlearrowright\rangle,|\circlearrowleft\rangle\}$, see the main text, and $D(x)=\exp[x(a-a^\dagger)]$ is the displacement operator.

The TLS truncation of the Rabi model gives for the gap $\omega_{10}=\omega_1-\omega_0$ of the effective TLS

$$\omega_{10} = \omega_{q,0} - \frac{\delta_1}{2} - \frac{1}{2}\sqrt{\delta_1^2+\Omega_1^2}\,. \tag{A18}$$

The relevant matrix elements are $Q_{l,01} = \langle 0|\hat{Q}_l|1\rangle$, where $\hat{Q}_L = a+a^\dagger$ and $\hat{Q}_R=\sigma_z$ (in the qubit localized basis). Using $D(x)aD^\dagger(x) = a+x$ and $D(x)a^\dagger D^\dagger(x) = (D(x)aD^\dagger(x))^\dagger = a^\dagger+x^*$, equations (A15) and (A17) give

$$Q_{L,01} = \frac{4g}{\omega_{\rm r}}\mathrm{u}_1^-c_0^-c_0^+ + \mathrm{v}_1^-\left(c_0^-c_1^- + c_0^+c_1^+\right)\,, \qquad Q_{R,01} = -2\mathrm{u}_1^-c_0^-c_0^+\,. \tag{A19}$$

A.2.2. Zero bias, $\epsilon=0$

The first two energy levels and the corresponding eigenstates read

$$\begin{aligned} \omega_0 &= -\frac{1}{2}\tilde{\Delta}_{00} - \frac{g^2}{\omega_{\rm r}}\,, \quad |0\rangle = |\Psi_{+,0}\rangle\,,\\ \omega_1 &= \frac{1}{2}\left(\frac{\tilde{\Delta}_{00}-\tilde{\Delta}_{11}}{2}+\omega_{\rm r}\right) - \frac{g^2}{\omega_{\rm r}} - \frac{1}{2}\sqrt{\left(\frac{\tilde{\Delta}_{00}+\tilde{\Delta}_{11}}{2}-\omega_{\rm r}\right)^2+\left(\tilde{\Delta}_{10}\right)^2}\,, \qquad |1\rangle = \mathrm{u}_1^-|\Psi_{-,0}\rangle + \mathrm{v}_1^-|\Psi_{+,1}\rangle\,, \end{aligned} \tag{A20}$$

and, since $c_j^\pm(\epsilon=0) = 1/\sqrt{2}$,

$$|\Psi_{\pm,j}\rangle = \frac{1}{\sqrt{2}}\left(|-_z j_-\rangle \pm |+_z j_+\rangle\right)\,. \tag{A21}$$

The gap $\omega_{10}=\omega_1-\omega_0$ of the effective qubit is

$$\omega_{10} = \tilde{\Delta} - \frac{1}{2}\left(\tilde{\Delta}-\omega_{\rm r}-\frac{\tilde{\alpha}\tilde{\Delta}}{2}\right) - \frac{1}{2}\sqrt{\left(\tilde{\Delta}-\omega_{\rm r}-\frac{\tilde{\alpha}\tilde{\Delta}}{2}\right)^2+\tilde{\alpha}\tilde{\Delta}^2}\,, \tag{A22}$$

where we have defined $\tilde{\Delta} := \Delta\exp(-\tilde{\alpha}/2) = \tilde{\Delta}_{00}$ and used $\tilde{\Delta}_{11} = \Delta\exp(-\tilde{\alpha}/2)(1-\tilde{\alpha})$ and $\tilde{\Delta}_{01} = \sqrt{\tilde{\alpha}}\tilde{\Delta}$. The matrix elements of $\hat{Q}_l$ in the basis $\{|0\rangle,|1\rangle\}$ read

$$Q_{L,01} = \frac{2g}{\omega_{\rm r}}\mathrm{u}_1^- + \mathrm{v}_1^-\,, \qquad Q_{R,01} = -\mathrm{u}_1^-\,. \tag{A23}$$

A.2.3. Weak coupling limit of the GRWA
To first order in $\tilde{\alpha}$, $\mathsf{L}_n^1(\tilde{\alpha}) \simeq n+1$ and $\mathsf{L}_n^0(\tilde{\alpha}) \simeq 1$. It follows that to first order in g

$$\begin{aligned}
\tilde{\Delta}_{nn} &\simeq \Delta\,, \\
\omega_{q,n} &\simeq \omega_{\mathrm{q}}\,, \\
c_n^{\pm} &\simeq \sqrt{\frac{\omega_{\mathrm{q}} \pm \epsilon}{2\omega_{\mathrm{q}}}}\,, \\
\Omega_n &\simeq \tilde{\Delta}_{nn-1} \simeq \Delta\sqrt{n\tilde{\alpha}}\,, \\
\delta_n &\simeq \omega_{\mathrm{q}} - \omega_{\mathrm{r}}\,.
\end{aligned} \tag{A24}$$

As a result, to first order in g, the spectrum acquires a form similar to that of the RWA, equation (A9).

$$\begin{aligned}
\omega_0 &\simeq -\omega_{\mathrm{q}}/2\,, \\
\omega_{2n-1} &\simeq \left(n-\frac{1}{2}\right)\omega_{\mathrm{r}} - \frac{1}{2}\sqrt{\left(\omega_{\mathrm{q}}-\omega_{\mathrm{r}}\right)^2 + n(\Delta\tilde{\alpha})^2}\,, \\
\omega_{2n} &\simeq \left(n-\frac{1}{2}\right)\omega_{\mathrm{r}} + \frac{1}{2}\sqrt{\left(\omega_{\mathrm{q}}-\omega_{\mathrm{r}}\right)^2 + n(\Delta\tilde{\alpha})^2}\,,
\end{aligned} \tag{A25}$$

the difference being that the term $\sqrt{\tilde{\alpha}}\Delta = 2\Delta g/\omega_{\mathrm{r}}$ is replaced in the RWA by $2g_x = 2\Delta g/\omega_{\mathrm{q}}$. The gap of the effective qubit reads

$$\omega_{10} = \frac{\omega_{\mathrm{q}}}{2} + \frac{\omega_{\mathrm{r}}}{2} - \frac{1}{2}\sqrt{\left(\omega_{\mathrm{q}}-\omega_{\mathrm{r}}\right)^2 + (\Delta\tilde{\alpha})^2}\,. \tag{A26}$$

The weak-coupling limit of the matrix elements for generic bias ϵ are given by equation (A19) and read

$$\begin{aligned}
Q_{L,01} &= \frac{2g}{\omega_{\mathrm{r}}}\mathrm{u}_1^-\frac{\Delta}{\omega_{\mathrm{q}}} + \mathrm{v}_1^-\,, \\
Q_{R,01} &= -\mathrm{u}_1^-\frac{\Delta}{\omega_{\mathrm{q}}}\,,
\end{aligned} \tag{A27}$$

where

$$\begin{aligned}
\mathrm{u}_1^- &= \frac{\omega_{\mathrm{q}}-\omega_{\mathrm{r}} - \sqrt{\left(\omega_{\mathrm{q}}-\omega_{\mathrm{r}}\right)^2 + (\Delta\tilde{\alpha})^2}}{\sqrt{\left(\omega_{\mathrm{q}}-\omega_{\mathrm{r}} - \sqrt{\left(\omega_{\mathrm{q}}-\omega_{\mathrm{r}}\right)^2 + (\Delta\tilde{\alpha})^2}\right)^2 + (\Delta\tilde{\alpha})^2}} \\
\mathrm{v}_1^- &= \frac{-\Delta\tilde{\alpha}}{\sqrt{\left(\omega_{\mathrm{q}}-\omega_{\mathrm{r}} - \sqrt{\left(\omega_{\mathrm{q}}-\omega_{\mathrm{r}}\right)^2 + (\Delta\tilde{\alpha})^2}\right)^2 + (\Delta\tilde{\alpha})^2}}\,.
\end{aligned} \tag{A28}$$

Appendix B. Coherence effects at the level of second order

Effects of coherence in the Rabi model are displayed by the steady-state transport also at the level of second order, i.e. at temperatures of the same order as the qubit parameter Δ. In the weak qubit–oscillator coupling regime, quasi-degeneracies in the spectrum at resonance, see figure 1(c), induce non-vanishing steady-state coherences which impact the conductance [37, 48, 54]. Figure 6 shows the same results for the thermal conductance as a function of the qubit bias ϵ as in figure 4. Here, we highlight the impact of coherence effects at the steady-state. Specifically, we compare in the main panel and in the inset, the results of the numerical evaluation with the full secular approximation, where coherences are neglected, with those from the partial secular master equation. In the latter, populations are coupled to the coherence ρ_{12} relative to the quasi-degenerate subspace. The conductance peaks calculated within the partial secular master equation show a suppression and a Lamb shift with respect to the one in the full secular approximation.

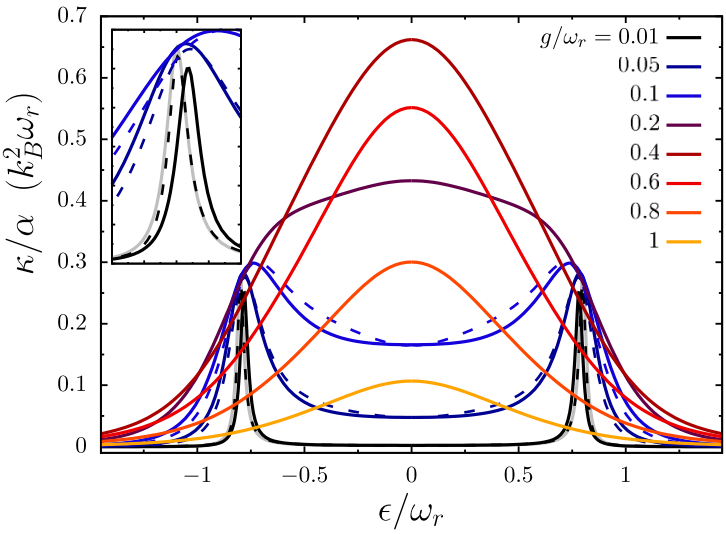

Figure 6. Conductance vs the qubit bias for different values of the coupling g. At weak coupling, the conductance exhibits two sharp peaks at resonance, $\omega_q = \omega_r$. As the coupling is increased, a broadened, zero-bias peak emerges. The quasi-degeneracy at resonance for small g, see figure 1(c), gives, in the partial secular master equation (black solid line) a suppressed peak with a Lamb shift, as highlighted in the inset. The gray solid line shows the conductance for $g/\omega_r = 0.01$ in the full secular approximation. Dashed lines: $\kappa^{(2)}$ in the full secular approximation within VVPT in g and truncation to the first four levels. The temperature is $k_B T = 0.2\,\hbar\omega_r$ and $\Delta/\omega_r = 0.6$.

ORCID iDs

L Magazzù https://orcid.org/0000-0002-4377-8387
E Paladino https://orcid.org/0000-0002-9929-3768
M Grifoni https://orcid.org/0000-0002-3534-8184

References

[1] Blais A, Grimsmo A L, Girvin S M and Wallraff A 2021 Circuit quantum electrodynamics *Rev. Mod. Phys.* **93** 025005
[2] Rabi I I 1936 On the process of space quantization *Phys. Rev.* **49** 324–8
[3] Rabi I I 1937 Space quantization in a gyrating magnetic field *Phys. Rev.* **51** 652–4
[4] Forn-Díaz P, Lisenfeld J, Marcos D, García-Ripoll J J, Solano E, Harmans C J P M and Mooij J E 2010 Observation of the Bloch-Siegert shift in a qubit-oscillator system in the ultrastrong coupling regime *Phys. Rev. Lett.* **105** 237001
[5] Yoshihara F, Fuse T, Ashhab S, Kakuyanagi K, Saito S and Semba K 2016 Superconducting qubit-oscillator circuit beyond the ultrastrong-coupling regime *Nat. Phys.* **13** 44
[6] Forn-Díaz P, Lamata L, Rico E, Kono J and Solano E 2019 Ultrastrong coupling regimes of light-matter interaction *Rev. Mod. Phys.* **91** 025005
[7] Kockum F A, Miranowicz A, De Liberato S, Savasta S and Nori F 2019 Ultrastrong coupling between light and matter *Nat. Rev. Phys.* **1** 19–40
[8] Falci G, Ridolfo A, Di Stefano P G and Paladino E 2019 Ultrastrong coupling probed by coherent population transfer *Sci. Rep.* **9** 9249
[9] Giannelli L, Paladino E, Grajcar M, Paraoanu G S and Falci G 2024 Detecting virtual photons in ultrastrongly coupled superconducting quantum circuits *Phys. Rev. Res.* **6** 013008
[10] Pekola J P and Karimi B 2021 Colloquium: quantum heat transport in condensed matter systems *Rev. Mod. Phys.* **93** 041001
[11] Gubaydullin A, Thomas G, Golubev D S, Lvov D, Peltonen J T and Pekola J P 2022 Photonic heat transport in three terminal superconducting circuit *Nat. Commun.* **13** 1552
[12] Upadhyay U, Golubev D S, Chang Y-C, Thomas G, Guthrie A, Peltonen J T and Pekola J P 2024 Microwave quantum diode *Nat. Commun.* **15** 630
[13] Ojanen T and Jauho A-P 2008 Mesoscopic photon heat transistor *Phys. Rev. Lett.* **100** 155902
[14] Ronzani A, Karimi B, Senior J, Chang Y-C, Peltonen J T, Chen C and Pekola J P 2018 Tunable photonic heat transport in a quantum heat valve *Nat. Phys.* **14** 991–5
[15] Segal D and Nitzan A 2005 Spin-boson thermal rectifier *Phys. Rev. Lett.* **94** 034301
[16] Segal D and Nitzan A 2005 Heat rectification in molecular junctions *J. Chem. Phys.* **122** 194704
[17] Segal D 2006 Heat flow in nonlinear molecular junctions: master equation analysis *Phys. Rev.* B **73** 205415
[18] Senior J, Gubaydullin A, Karimi B, Peltonen J T, Ankerhold J and Pekola J P 2020 Heat rectification via a superconducting artificial atom *Commun. Phys.* **3** 40
[19] Bhandari B, Erdman P A, Fazio R, Paladino E and Taddei F 2021 Thermal rectification through a nonlinear quantum resonator *Phys. Rev.* B **103** 155434
[20] Tesser L, Bhandari B, Erdman P A, Paladino E, Fazio R and Taddei F 2022 Heat rectification through single and coupled quantum dots *New J. Phys.* **24** 035001

[21] Leggett A J, Chakravarty S, Dorsey A T, Fisher M P A, Garg A and Zwerger W 1987 Dynamics of the dissipative two-state system *Rev. Mod. Phys.* **59** 1–85
[22] Weiss U 2012 *Quantum Dissipative Systems* 4th edn (World Scientific)
[23] Ruokola T and Ojanen T 2011 Thermal conductance in a spin-boson model: cotunneling and low-temperature properties *Phys. Rev.* B **83** 045417
[24] Nicolin L and Segal D 2011 Non-equilibrium spin-boson model: counting statistics and the heat exchange fluctuation theorem *J. Chem. Phys.* **135** 164106
[25] Saito K and Kato T 2013 Kondo Signature in heat transfer via a local two-state system *Phys. Rev. Lett.* **111** 214301
[26] Yang Y and Wu C-Q 2014 Quantum heat transport in a spin-boson nanojunction: coherent and incoherent mechanisms *Europhys. Lett.* **107** 30003
[27] Thingna J, Zhou H and Wang J-S 2014 Improved Dyson series expansion for steady-state quantum transport beyond the weak coupling limit: divergences and resolution *J. Chem. Phys.* **141** 194101
[28] Wang C, Ren J and Cao J 2015 Nonequilibrium energy transfer at nanoscale: a unified theory from weak to strong coupling *Sci. Rep.* **5** 11787
[29] Xu D and Cao J 2016 Non-canonical distribution and non-equilibrium transport beyond weak system-bath coupling regime: a polaron transformation approach *Front. Phys.* **11** 110308
[30] Wang C, Ren J and Cao J 2017 Unifying quantum heat transfer in a nonequilibrium spin-boson model with full counting statistics *Phys. Rev.* A **95** 023610
[31] Yamamoto T, Kato M, Kato T and Saito K 2018 Heat transport via a local two-state system near thermal equilibrium *New J. Phys.* **20** 093014
[32] Chen Z-H, Che H-X, Chen Z-K, Wang C and Ren J 2022 Tuning nonequilibrium heat current and two-photon statistics via composite qubit-resonator interaction *Phys. Rev. Res.* **4** 013152
[33] Xu M, Stockburger J T and Ankerhold J 2021 Heat transport through a superconducting artificial atom *Phys. Rev.* B **103** 104304
[34] Yamamoto T and Kato T 2021 Heat transport through a two-level system embedded between two harmonic resonators *J. Phys.: Condens. Matter* **33** 395303
[35] Garg A, Onuchic J N and Ambegaokar V 1985 Effect of friction on electron transfer in biomolecules *J. Chem. Phys.* **83** 4491–503
[36] Magazzù L and Grifoni M 2019 Transmission spectra of an ultrastrongly coupled qubit-dissipative resonator system *J. Stat. Mech.* 104002
[37] Magazzù L, Paladino E and Grifoni M 2024 Unified diagrammatic approach to quantum transport in few-level junctions for bosonic and fermionic reservoirs: application to the quantum Rabi model *Phys. Rev.* B **110** 085419
[38] Ashhab S and Nori F 2010 Qubit-oscillator systems in the ultrastrong-coupling regime and their potential for preparing nonclassical states *Phys. Rev.* A **81** 042311
[39] Hausinger J and Grifoni M 2008 Dissipative dynamics of a biased qubit coupled to a harmonic oscillator: analytical results beyond the rotating wave approximation *New J. Phys.* **10** 115015
[40] Twyeffort Irish E K 2007 Generalized rotating-wave approximation for arbitrarily large coupling *Phys. Rev. Lett.* **99** 173601
[41] Zhang Y-Y, Chen Q-H and Zhao Y 2013 Generalized rotating-wave approximation to biased qubit-oscillator systems *Phys. Rev.* A **87** 033827
[42] Zueco D and García-Ripoll J J 2019 Ultrastrongly dissipative quantum Rabi model *Phys. Rev.* A **99** 013807
[43] Magazzù L, Forn-Díaz P and Grifoni M 2021 Transmission spectra of the driven, dissipative Rabi model in the ultrastrong-coupling regime *Phys. Rev.* A **104** 053711
[44] Caldeira A O and Leggett A J 1981 Influence of dissipation on quantum tunneling in macroscopic systems *Phys. Rev. Lett.* **46** 211–4
[45] Caldeira A O and Leggett A J 1983 Quantum tunnelling in a dissipative system *Ann. Phys., NY* **149** 374–456
[46] Donarini A and Grifoni M 2024 *Quantum Transport in Interacting Nanojunctions: a Density Matrix Approach* (Springer)
[47] Thingna J, Garcí-a-Palacios J L and Wang J-S 2012 Steady-state thermal transport in anharmonic systems: application to molecular junctions *Phys. Rev.* B **85** 195452
[48] Ivander F, Anto-Sztrikacs N and Segal D 2022 Quantum coherence-control of thermal energy transport: the V model as a case study *New J. Phys.* **24** 103010
[49] Karimi B and Pekola J P 2016 Otto refrigerator based on a superconducting qubit: classical and quantum performance *Phys. Rev.* B **94** 184503
[50] Karimi B, Pekola J P, Campisi M and Fazio R 2017 Coupled qubits as a quantum heat switch *Quantum Sci. Technol.* **2** 044007
[51] Rasmussen S E, Christensen K S, Pedersen S P, Kristensen L B, Bækkegaard T, Loft N J S and Zinner N T 2021 Superconducting circuit companion—an introduction with worked examples *PRX Quantum* **2** 040204
[52] Iorio A, Strambini E, Haack G, Campisi M and Giazotto F 2021 Photonic heat rectification in a system of coupled qubits *Phys. Rev. Appl.* **15** 054050
[53] Shore B W and Knight P L 1993 The Jaynes-Cummings model *J. Mod. Opt.* **40** 1195–238
[54] Cattaneo M, Giorgi G L, Maniscalco S and Zambrini R 2019 Local versus global master equation with common and separate baths: superiority of the global approach in partial secular approximation *New J. Phys.* **21** 113045